Estimating reservoir permeability with borehole radar

(February 2, 2020)

Running head: **Borehole radar permeability estimation**

ABSTRACT

In oil drilling, mud filtrate penetrates into porous formations and alters the compositions and properties of the pore fluids. This disturbs the logging signals and brings errors to reservoir evaluation. Drilling and logging engineers therefore deem mud invasion as undesired, and attempt to eliminate its impacts. However, the mud-contaminated formation carries valuable information, notably with regard to its key hydraulic properties. Typically, the invasion depth critically depends on the formation porosity and permeability. Therefore, if adequately characterized, mud invasion effects could be utilized for reservoir evaluation. To pursue this objective, we apply borehole radar to measure mud invasion depth considering its high radial spatial resolution compared with conventional logging tools, which then allows us to estimate the reservoir permeability based on the acquired invasion depth. We investigate the feasibility of this strategy numerically through coupled electromagnetic and fluid modeling in an oil-bearing layer drilled using freshwater based mud. Time-lapse logging is simulated to extract the signals reflected from the invasion front, and a dual-offset downhole antenna mode enables time-to-depth conversion to determine the invasion depth. Based on drilling, coring, and logging data, a quantitative interpretation chart is established, mapping porosity, permeability, and initial water saturation into invasion depth. The estimated permeability

is in a good agreement with the actual formation permeability. The results of this work thus suggest that borehole radar has significant potential to estimate permeability through mud invasion effects. Ground-penetrating radar has found a novel application in reservoir evaluation.

INTRODUCTION

Porosity, permeability, and water saturation are essential petrophysical properties in hydrocarbon reservoir evaluation. Water saturation and porosity can be reliably inferred by conventional well logging data, whereas permeability information is notoriously difficult to be directly estimated downhole (Darling, 2005). Permeability has complex relations with other petrophysical properties and is generally associated with grain size, pore size, specific surface area, pore throat size, and porosity connectivity (Yao and Holditch, 1993). Core analysis is deemed the most direct and reliable way to determine permeability. However, it is costly and is therefore generally limited to a few stratigraphic locations (Donaldson and Clydesdale, 1990). In addition, to uncertainties and/or biases in sampling, core samples are measured in a laboratory environment, which is not guaranteed to be equivalent with the in-situ (Ahmed et al., 1991). Furthermore, core measurements are carried out at a scale that is not representative of the fluid flow in a representative elementary volume (REV) of the reservoir (Glover et al., 2006). Some empirical models have been established to estimate permeability from porosity through statistical correlations, typically based on the Kozeny-Carman equation (Zunker, 1930; Carman, 1956; Timur, 1968; Coates et al., 1973; Nooruddin and Hossain, 2011). The validity of these methods is based on premise of a close correlation between the permeability and porosity. However, for some pertinent reservoir types, for example, those with low porosity and low permeability, it is generally acknowledged that the correlation between the porosity and permeability tends to be poor to non-existent. The reason for this is that geometry and specific surface of the pores have more significant effects on the permeability than the pore size itself does (Ahmed et al., 1991). Field-based core analysis shows that, in low-porosity reservoirs, the permeability may fluctuate by orders of magnitude even if

the porosity is quasi-constant (Sirait, 2015). Moreover, in consolidated sandstone, fractured, and karstic reservoirs, there are rarely consistent correlations between the porosity and permeability (Grude et al., 2014). Similarly, permeability estimation based on the analysis of Stonely waves and Nuclear Magnetic Resonance (NMR) logging is generally invalid in low-porosity reservoirs (Tang and Cheng, 1996; Weller et al., 2010).

In the course of the drilling, mud filtrate penetrates into the porous formation, and alters the compositions of the pore fluids. This brings about disturbances in well logging signals and affects the accurate evaluation of reservoir properties. Logging engineers try to eliminate mud invasion effects and to accordingly correct the logging data. Nevertheless, the mud-contaminated parts of the formation could contain some valuable information. A parametric sensitivity analysis revealed that for a given formation interval, the invasion depth has strong correlations with the permeability and porosity (Zhou et al., 2015). This inspires us to find a new approach to estimate the hydraulic properties of a reservoir based on the mud invasion effects. The feasibility of this approach relies on two principal considerations: one is that the mud invasion effects, especially the invasion depth, can be characterized adequately by well logging; the other is that a quantitative relationship should be established to link the invasion effects with the formation properties. A few numerical and field trials attempted to estimate the reservoir permeability by inverting the radial electrical resistivity profiles, inferred from array induction logging, of an invaded reservoir (Alpak et al., 2006; Torres-Verdín et al., 2006; Zhou et al., 2016). The estimated results provided consistent order-of-magnitude-type with the coring permeability, but the errors are considerable. This is due to the fact that array induction logging has a too low radial spatial resolution to precisely solve the invasion depth. Conventional logging methods, whether electrical or acoustic, have no capability of finely describing the

complicated invasion status due to their limited resolution and/or sensitivity. To alleviate this problem, the use of high-frequency borehole radar for detecting mud invasion depth is investigated in this paper. Once the invasion depth is accurately identified by borehole radar measurements, we can then correlate it with the reservoir permeability.

Borehole radar has been widely applied in shallow surface mining, cavity imaging, fracture characterization, and hydrogeophysical exploration (Fullagar et al., 2000; Tronicke et al., 2004; Zhou and Sato, 2004; Zhao and Sato, 2006; Liu et al., 2019). Chen and Oristaglio (2002) firstly proposed to apply borehole radar to well logging. Miorali et al. (2011) and Zhou et al. (2018) proposed to apply borehole radar to monitor water-oil movement for oil production optimization. A borehole radar logging prototype has been developed with the original intention to image fractures in hydrocarbon reservoirs (Liu et al., 2012; Liang et al., 2012; Ma et al., 2016). The aforementioned borehole radar applications operate at frequencies of a few hundred MHz, which correspond to wavelengths in decimeter to meter range and penetrate the reservoirs in a range of a few meters. Oloumi et al. (2015, 2016) conducted laboratory experiments to investigate the feasibility of characterizing the oil well perforation and corrosion with the near-field responses of a high frequency (up to 6 GHz) radar antenna. Hizem et al. (2008) introduced a dielectric logging tool consisting of multi-spacing and multi-frequency (from 20 MHz to 1 GHz) coils to characterize the near-borehole region. However, the narrow-band signals and short offsets limit the accuracy and integrity of the acquired information. For the mud invasion detection purposes, a penetrating depth of tens of centimeters and radial resolution of a few centimeters are required. Heigl and Peeters (2005) numerically simulated high-frequency radar wave propagation and reflection in oil-based and water-based mud invasion cases. They suggested that a directional borehole

97 wide-band radar with a center frequency of 1 GHz is able to detect observable signals
98 reflected from mud invasion front, even under the relatively conservative limitations on
99 radar system performance. Although Heigl and Peeters (2005) built up a simplified
100 geological model in the study, we believe that their suggested radar frequency is applicable
101 for realistic reservoir environments.

102 To our knowledge, such radar logging tools do not exist for the purpose of mud
103 invasion detection. We therefore present a numerical study that investigates the feasibility
104 of detecting mud invasion and estimating permeability using borehole radar. The
105 proposed method couples a hydraulic model with a solution of the electromagnetic
106 equations in an effort to realistically replicate the radar responses on a mud-disturbed
107 reservoir. We simulate a scenario of freshwater mud invading a low-permeability oil
108 reservoir with open-hole radar logging to explore the feasibility of the proposed method.

NUMERICAL MODELING

109 Mud invasion modeling and reservoir scenario

110 Mud invasion is a complicated flow and transport process, specific to drilling mud types
111 and reservoir conditions. Generally, logging engineers divide the invaded formation into the
112 flushed, transition, and virgin (or undisturbed) zones according to how much mobile in-situ
113 fluids are displaced by mud filtrate (Salazar and Torres-Verdín, 2008). To acquire detectable
114 radar reflections from the invasion front, several crucial factors should be considered. First,
115 the flushed zone should have a relatively low conductivity to ensure low attenuation and low
116 phase distortion for radar wave propagation. Second, there must be an adequate contrast of
117 electrical properties between the flushed and virgin zones, and the transition zone should be

thin and exhibit a steep gradient relative to the dominant wavelength, such that sufficiently strong radar reflection events are generated.

Drilling mud types are usually categorized into freshwater mud, saltwater mud and oil-based mud (Fink, 2015). Salt water mud brings about a highly conductive flushed zone, which would compromise the performance of borehole radar by severely reducing its penetration depth. Oil-based mud is favorable for radar wave propagation because of the associated low conductivity of the invaded zones. It does, however, tend to create a gradual oil-water transition zone primarily due to the non-wettability and the low flow coefficient of the oleic phase (Salazar and Torres-Verdín, 2008). The resulting gradual transition zone is unfavorable for generating radar wave reflections in our borehole radar applications. Besides, oil-based mud is not as popular as water-based mud due to its high costs and environmental unfriendliness (Fink, 2015). Therefore, we prefer to consider freshwater mud for the purpose of this study.

Reservoirs frequently consist of one sand body sandwiched between gas- and brine-saturated sections (Van Lookeren, 1965). In a completely water-saturated layer, the invaded water-based mud filtrate is miscible with the in-situ aqueous phase and, hence, it is difficult to explicitly define an invasion boundary. Therefore, we restrict the current investigations to an oil-bearing layer because of the immiscibility of aqueous and oleic phases. A heavy oil reservoir is not recommended for the proposed borehole radar applications due to the fact that the high viscosity of the oleic phase creates a gradual and long transition zone, which is not favorable for radar wave propagation and reflection (Zhou, 2011). For these considerations, the current investigation is carried out in a scenario of freshwater mud invading a light-oil layer.

The physical process of mud invasion is usually described as a multiphase and multicomponent flow problem (Gunawan et al., 2011). We adopt the two-phase (water and oil) isothermal Darcy flow equations and convection-diffusion equation to solve for the pressure, water saturation, and water salinity in the near-borehole region over invasion time (Aziz, 1979; Delshad and Pope, 1989; George et al., 2003). The equation sets are discretized in a cylindrical coordinate system, and pressure, saturation, and salinity are sequentially solved for with the implicit, explicit, and implicit treatments, respectively. We understand that the characteristics of the shape of fluid distribution are critical to investigate the radar wave propagation, transmission, and reflection. Therefore, our model incorporates as many parameters as possible, such as capillary pressure, rock and fluid compressibility, and ionic diffusion effect, in order to simulate realistic fluid transition profiles. Localized grid refinement is employed in the near-borehole region.

The drilling mud generally contains solid particles to sustain a slightly high downhole pressure with respect to the reservoir. In the course of the mud invasion, the solid particles gradually deposit on the borehole wall and build up a so-called mud cake (Wu et al., 2005). The temporal evolution of mud cake thickness, permeability, and porosity depends on the pressure drop across the mud cake in addition to the textures of the mud itself. Correspondingly, the time-varying mud cake properties influence the inflow rate and, thus, the invasion depth at a given time. Essentially, the flow coefficients of fluids in the mud cake and the formation tend to control the invasion rate under a certain pressure difference (Salazar and Torres-Verdín, 2008). To emulate this process, a set of mud cake growth formulas derived based on laboratory experiments (Wu et al., 2005), are coupled with the above flow modeling outlined above. We developed a 2D MATLAB®* program for the

*Trademark of The MathWorks, inc.

mud invasion simulations, which has shown to agree well with the published commercial soft-based results (Zhou et al., 2016).

We simulate a scenario of fresh water mud invading a light oil layer. The governing parameters and material properties are listed in Table 1. The considered porosity, permeability, and water saturation curves, which vary with depth, are synthesized based on core data from a well in the Honghe Oilfield, Ordos Basin, China. The results shown in Figure 1 are obtained after applying a 5-point moving average filter to reduce erratic noise. This oil field is a typical tight oil sandstone reservoir, which presents an ideal test scenario for our study: first, the considered reservoir section is characterized by low porosity and low permeability, which means that the permeability can not be accurately estimated through the correlations with porosity; second, the selected layer contains a high percentage of oil, which would form a distinct oil-water front in the course of the invasion process.

[Table 1 about here.]

[Figure 1 about here.]

Borehole radar configuration and modeling

Compared with surface ground-penetrating radar measurements, borehole radar logging works in a complex environment, which, in turn, imposes constraints on the antenna configurations (Slob et al., 2010). To carry out the downhole measurements, the radar antennas are mounted in an arc-shaped cavity of the logging string. To decrease the interference arising from the metal components and increase the radar directionality, a

certain special material is filled in the cavity. There are two optional schemes for the filling material. One is to choose a material with a high dielectric permittivity, thus, shortening the wavelength of the backscattered waves to decrease the destructive interference (Miorali et al., 2010); the other is to use a type of absorbing material to attenuate the backscattered waves (Liang et al., 2012). We adopt the latter scheme by filling absorbing material into the cavity. The filling material should have certain dielectric permittivity loss or magnetic permeability loss to convert the backscattered energy into heat. Ferrite is an often used material for this purpose, especially in borehole radars, because it has large mechanical strength as well as high dielectric and magnetic losses in the working frequency band of ground-penetrating radar (Chen et al., 2002). We set the material properties in our model as shown in Table 2, simulating a sintered nickel zinc ferrite material (Liu, 2014). The absorbing effect in the considered radar frequency range is not optimal but still adequately effective. The downhole transreceiver configuration is designed as a one-transmitting and two-receiving mode, which, resembling the common depth point measurement on the surface, facilitates a time-to-depth conversion for invasion depth estimation. A Ricker wavelet with a center frequency of 1 GHz is exerted on the transmitting antenna. This frequency range satisfies the penetration depth and spatial resolution required in a high-resistivity reservoir (Heigl and Peeters, 2005). A backward caliper arm in the logging string can push the antennas against the borehole wall in order to eliminate attenuation and scattering loss caused by the conductive mud. Similar caliper arm configurations have been used in density logging, micro-resistivity logging and dielectric logging tools, where it is required to directionally inject energy into the formation in an open hole (Crain, 2002; Hizem et al., 2008).

We use gprMax, a general purpose finite-difference time-domain (FDTD)

ground-penetrating radar simulator (Warren et al., 2016), to build up a borehole radar model for a mud-filled downhole environment. The antennas are modeled as Hertzian dipoles with the polarization direction parallel to the borehole. This configuration is used as an approximation to the wire dipole antennas designed by Sato and Miwa (2000). We choose the electrical field component parallel to the borehole as the received signals. The FDTD grid has a uniform spatial step with 2 mm on the side, and the time step is chosen based on the Courant limit (Taflove and Hagness, 2005). Perfectly matched layers are imposed in the domain boundaries to simulate an infinite propagation space (Giannopoulos, 2012; Giannakis and Giannopoulos, 2014).

The porosity as well as the water saturation and salinity are initially extracted from the mud invasion simulations. Subsequently, the aforementioned properties are converted to bulk permittivity and conductivity and are implemented into the radar model. To that end, two formulas for the electrical property calculations of the mixed materials are employed to couple the radar and flow models. Archie's law is a good approximation to calculate the bulk electrical conductivity in our scenario of a resistive sandstone-type reservoir (Archie, 1942):

$$\sigma = \frac{\sigma_{\mathrm{w}} \phi^m S_{\mathrm{w}}^n}{\alpha}, \tag{1}$$

where σ and σ_{w} denote the bulk conductivity of the saturated rock and formation water conductivity (S/m), respectively; ϕ and S_{w} stand for the porosity and water saturation (fraction), respectively; m, n and α are the cementation, saturation exponents and tortuosity factor, respectively, which are empirical constants measured on core samples and defined in Table 2. In the above equation, the formation water conductivity is

calculated as a function of temperature and salinity (Bateman and Konen, 1978):

$$\sigma_{\mathrm{w}} = [(0.0123 + \frac{3647.5}{C_{\mathrm{w}}^{0.995}})\frac{82}{1.8T + 39}]^{-1}, \tag{2}$$

where C_{w} and T denotes the formation salinity (ppm) and temperature (°C). The bulk permittivity is calculated with the permittivities of the dry rock matrix, water, and oil and their respective volume fractions through the complex refractive index model (CRIM) (Birchak et al., 1974):

$$\sqrt{\varepsilon} = \sqrt{\varepsilon_{\mathrm{m}}}(1 - \phi) + \sqrt{\varepsilon_{\mathrm{o}}}(\phi - \phi S_{\mathrm{w}}) + \sqrt{\varepsilon_{\mathrm{w}}}\phi S_{\mathrm{w}}, \tag{3}$$

where ε, ε_{m}, ε_{o}, and ε_{w} denotes the bulk permittivity of the saturated rock, dry rock matrix permittivity, oil permittivity and water permittivity, respectively. CRIM is a widely used dielectric mixing formula, and it is still valid in reservoir environments when the frequency is relatively high (> 100 MHz) and interfacial polarization does not occur (Hizem et al., 2008). Under the deep reservoir environments, the relative permittivity of water, which is 81 under ambient conditions, should be modified. Donadille and Faivre (2015) carried out laboratory measurements of water permittivity under the condition of high temperature, high pressure, and high salinity, and revealed that temperature has a major impact on water permittivity, and salinity has a moderate impact on it, whereas pressure effects can be neglected. We include the salinity and temperature effects on the water permittivity in our CRIM model through a polynomial interpolation of the laboratory data measured by Donadille and Faivre (2015), as depicted in Figure 2. Considerable differences with regard to the surface ground-penetrating radar measurements are that water relative permittivity drops to approximately 58 at the temperature of approximate 100 °C, and its magnitude decreases with the increase of the water salinity. Besides, water permittivity becomes frequency independent in our applied radar frequency range because the relaxation

frequency shifts to approximately 50 GHz as the temperature rises to 100 °C, implying that the dipole losses within water can be considered negligible (Hizem et al., 2008).

[Figure 2 about here.]

The downhole antenna configurations and the coupled fluid flow model are illustrated in Figure 3. The geometric parameters of the borehole radar and the material properties of the borehole and the reservoir are presented in Table 2. Through the coupling of the flow and radar models, a real-time borehole radar response of invasion process can be simulated.

[Figure 3 about here.]

[Table 2 about here.]

Fluid distributions and radar responses

The spatial distributions of the fluid and electrical properties during the invasion process are derived from the mud invasion simulations. Figure 4 shows the 2D fluid and electrical property distributions after 36 hours of invasion, and Figure 5 compares the radial fluid and electrical property curves after 36 and 60 hours. We can see that the invaded reservoir presents a relatively flat flushed zone and a sharp transition zone, which is favorable for radar wave propagation and reflection. Recall that we simulate a light oil reservoir scenario, where a low oil-water viscosity ratio takes primary responsibility for the piston-like invasion profile. We also see that the evolution of water salinity lags behind the water saturation. This phenomenon is caused by the diffusion and dispersion of the different saline concentrations between the in-situ formation water and the invading mud water. The lag effect is thought

to take responsibility for the so-called low-resistivity annulus (i.e., the high-conductivity annulus in Figure 5) (Salazar and Torres-Verdín, 2008). We observe that the evolution of the conductivity over time is consistent with that of the water salinity, while the permittivity with the water saturation. Note that an abnormal drop in the relative permittivity curve is caused by the impact of the salinity on the water permittivity. From the character of electrical property profiles, we expect that the significant radar wave reflection events are largely governed by the discontinuity of the conductivity distribution rather than by that of the permittivity.

Comparing the shapes of the invasion profiles at different times, we find that the electrical properties of the flushed zone change much less over invasion time than those of the transition zone. Therefore, we propose to perform time-lapse logging measurements to extract the reflected signals from the transition zone. Time-lapse logging has proven to be effective for extracting information with regard to changes in the rock physical properties especially when applied to fluid flow monitoring (Murphy and Owens, 1964). Miorali et al. (2011) and Zhou et al. (2018) have used time-lapse borehole radar measurements to extract the reflected signals from the water-oil contact. In our case, time-lapse logging is expected to filter out the majority of the direct wave as well as the the clutter arising from the heterogeneous rock properties. We implement time-lapse operations between times of 36 and 60 hours and record the time-lapse radar signals at two receivers as shown in Figure 6. There are three events observed in each radar profile. The first one close to the wellbore is caused by the changes in the near-borehole fluid content and the mud cake properties. These changes are minimal. However, because they are closely adjacent to the antennas, strong time-lapse signals are generated. The other two reflection events come from the invasion transition zone at 36 and 60 hours, respectively. The choice of the

logging times is based on the consideration that it should allow for separating different events. In practice, to acquire high-quality time-lapse signals, it is crucial to keep a relatively small shift of the locations of antennas in the radial and azimuthal directions for each sequential logging operation.

[Figure 4 about here.]

[Figure 5 about here.]

[Figure 6 about here.]

PERMEABILITY ESTIMATION

Estimation of invasion depth

We configure the receiving radar antennas with two different offsets in the logging string (Figure 3), which allows for time-to-depth conversion. The depth and wave velocity are simultaneously determined using the equations

$$\begin{cases} 2\sqrt{(l_1/2)^2 + {d_x}^2} = v_x(t_1 - \tau), \\ 2\sqrt{(l_2/2)^2 + {d_x}^2} = v_x(t_2 - \tau), \end{cases} \tag{4}$$

where l_1 and l_2 are the known offsets of the transmitting and receiving antennas, respectively, t_1 and t_2 denote the picked travel times of the reflected wavelets in the two receivers, τ is half of the time period of the source wavelength in the transmitter, and v_x and d_x are respectively the average wave velocity and the invasion depth, which are to be solved in the equations. The spacings l_1 and l_2 between the transmitting and receiving antennas are defined in Table 2 and designed to be comparable with the invasion depth

range. The travel times t_1 and t_2 of the reflected signals are picked up from the peaks of the wavelets of the second event (Figure 6). It is important to note that the travel times of the reflected signals should be calibrated by the period of the half wavelength (τ), because the real starting time of the source wavelet is difficult to pick with confidence. To estimate the period of the half-wavelength, we extract the time of the peaks of the direct waves in the radar data from the two receivers prior to the time-lapse difference operations and then solve for τ by setting d=0 in equation 4.

Figure 7 compares the invasion depth estimated from the radar data and the conductivity distribution simulated from fluid flow model. It can be seen that the estimated invasion depth is located at the starting point of the high conductivity annulus, which verifies that the reflection events occur at the discontinuity of the conductivity as predicted above. The agreement implies that the proposed mud invasion characterization approach is capable of estimating the invasion depth effectively and accurately.

[Figure 7 about here.]

Estimating permeability

Generally, the properties related to fluids, such as viscosity, compressibility, relative permeability curves, and capillary pressure features, in a given reservoir interval are constant, whereas the permeability, porosity, and initial water saturation vary with reservoir depth (Torres-Verdín et al., 2006). The reservoir permeability and mud cake permeability both affect the inflow rate of the mud filtrate (Salazar and Torres-Verdín, 2008). Therefore, a high formation permeability normally causes a large invasion rate and thus a large invasion volume at a certain invasion time. Formation porosity per se does

not influence the invasion rate if its correlation with the permeability is ignored. Under this assumption, a lower porosity leads to a larger invasion depth for a given invasion volume because the smaller pores require a larger invasion depth to contain the same volume of fluids. Initial water saturation has no straightforward correlation with the invasion rate. However, the water saturation determines the capillary pressure and relative permeabilities (Delshad and Pope, 1989), which implicitly relates the initial water saturation with the invasion rate. A systematic analysis of the parametric sensitivity revealed the following relationships of the invasion depth and the reservoir properties (Zhou et al., 2015, 2016): (1) There exists a strong correlation between the invasion depth and the permeability in low-permeability reservoirs. However, the correlation becomes poor when the reservoir permeability is large. This is because a high reservoir permeability leads to a large pressure drop across the mud cake, which increases the mud cake permeability due to the mud cake compressibility and makes it dominant in the invasion rate (Wu et al., 2005). (2) Porosity has a negative correlation with the invasion depth because a high porosity means a short length to contain the same filtrate volume, and the invasion depth is more sensitive to a low porosity reservoir than a high one. (3) Initial water saturation has a minor influence on the invasion depth, but a high initial water saturation tends to form an indistinctive contrast between the flushed and virgin zones. Correlation analysis implied that one can estimate reservoir permeability with the obtained invasion depth once the porosity and water saturation, as well as the drilling and coring data, are available.

A 4D interpretation chart can be used for estimating the reservoir permeability, for which a sequence of mud invasion simulations are required to map varying porosity, permeability, and initial water saturation values to their corresponding invasion depths.

The interpretation chart assumes that the properties of mud cake, fluids and formation are available as prior knowledge. In practical field applications, the mud and mud cake parameters are determined by the drilling fluid configuration scheme. Core sample analysis can acquire the fluid and rock properties, e.g., capillary pressure, relative permeabilities, viscosities, and rock-electric properties. Conventional logging can obtain the initial water saturation, pressure, porosity, and temperature of the reservoir. When the borehole radar solves the invasion depth, permeability can be estimated through the interpretation chart. Figure 8 illustrates the corresponding work flow.

[Figure 8 about here.]

Figure 9 presents the 4D interpretation chart based on our reservoir scenario after 36 hours of mud invasion, and Figure 10 extracts 1D curves from Figure 9 showing how the permeability, porosity, and initial water saturation independently influence the invasion depth. We observe that (1) the initial water saturation has unnoticeable effects on the invasion depth; (2) the porosity has a negative correlation with the invasion depth; (3) the permeability has a high correlation with the invasion depth and the correlation dramatically drops when the permeability increases to a few md. The observed phenomena coincide with our previous parametric sensitivity analysis of mud invasion (Zhou et al., 2015), and suggest that the proposed method is limited in low-porosity and low-permeability reservoirs.

[Figure 9 about here.]

[Figure 10 about here.]

With the invasion depth acquired through borehole radar logging (Figure 11a), we estimate the permeability based on the calibrated data in Figure 9a. The corresponding

results are presented in Figure 11b. Compared with the preset permeability curves, the estimated permeability curve shows a good agreement. The discrepancies are mainly caused by the decimal precision limit of 0.01 that we impose on the initial water saturation and porosity as the variables imported into the interpretation chart, imitating the imperfect data measurements of the conventional logging in practice. Besides, it can bee seen that the absolute errors in the high permeability segments (i.e., the two peaks) are higher than those in the low permeability ones, which proves that the proposed method is better suited to lower permeability intervals.

[Figure 11 about here.]

The simulation results imply that, in principle, the permeability can be estimated based on the mud invasion depth inferred from borehole radar measurements. However, an accurate permeability estimation heavily relies on the comprehensive collection and precise analysis of drilling, coring, and logging data. In practical borehole radar logging, the instrument operations and signal processing methods affect the accuracy and precision of the proposed method. An ideal application environment of borehole radar is a low-porosity and low-permeability hydrocarbon reservoir drilled using freshwater mud and followed by open-hole logging. Future work will include sensitivity analyses to the error sources and the recommendations on how to make this approach more viable for practical applications.

CONCLUSIONS

A new method is proposed to estimate reservoir permeability via the mud invasion depth detected by borehole radar. The measurement configuration consists of two receivers and

401 one transmitter operating at 1 GHz center frequency. Time-lapse measurements are
402 employed to effectively extract the reflected signals from the invasion front. The
403 permeability is estimated based on interpretation charts that relate the invasion depth
404 with the petrophysical properties of the reservoir. A numerical study is presented, which
405 couples fluid flow and radar modeling in order to accurately simulate the investigated
406 scenario consisting of a low-porosity and low-permeability reservoir drilled using
407 freshwater mud. The results indicate that borehole radar has potential to allow for the
408 estimation of the invasion depth and thus for the permeability. We expect that our study
409 will explore a potential application of ground-penetrating radar in oil fields, as well as an
410 effective solution for permeability estimation problem.

ACKNOWLEDGMENTS

REFERENCES

411 Ahmed, U., S. Crary, and G. Coates, 1991, Permeability estimation: The various sources
412 and their interrelationships: Journal of Petroleum Technology, **43**, 578–587.

413 Alpak, F. O., C. Torres-Verdín, and T. M. Habashy, 2006, Petrophysical inversion of
414 borehole array-induction logs: Part I–Numerical examples: Geophysics, **71**, no. 4, F101–
415 F119.

416 Archie, G. E., 1942, The electrical resistivity log as an aid in determining some
417 reservoir characteristics: Transaction of American Institute of Mining, Metallurgical,
418 and Petroleum Engineers, **146**, 54–62.

419 Aziz, K., 1979, Petroleum reservoir simulation: Applied Science Publishers.

420 Bateman, R. M., and C. E. Konen, 1978, The log analyst and the programmable pocket
421 calculator: The Log Analyst, **19**.

422 Birchak, J. R., C. G. Gardner, J. E. Hipp, and J. M. Victor, 1974, High dielectric constant
423 microwave probes for sensing soil moisture: Proceedings of the IEEE, **62**, 93–98.

424 Carman, P. C., 1956, Flow of gases through porous media: Butterworths.

425 Chen, Y., R. T. Coates, and W. C. Chew, 2002, FDTD modeling and analysis of a broadband
426 antenna suitable for oil-field imaging while drilling: IEEE Transactions on Geoscience and
427 Remote Sensing, **40**, 434–442.

428 Chen, Y., and M. L. Oristaglio, 2002, A modeling study of borehole radar for oil-field
429 applications: Geophysics, **67**, 1486–1494.

430 Coates, G. R., J. Dumanoir, et al., 1973, A new approach to improved log-derived
431 permeability: Presented at the SPWLA 14th Annual Logging Symposium, Society of
432 Petrophysicists and Well-Log Analysts.

433 Crain, E. R., 2002, Crain's petrophysical handbook: Rocky Mountain House.

Darling, T., 2005, Well logging and formation evaluation: Elsevier.

Delshad, M., and G. A. Pope, 1989, Comparison of the three-phase oil relative permeability models: Transport in Porous Media, **4**, 59–83.

Donadille, J., and O. Faivre, 2015, Water complex permittivity model for dielectric logging: Presented at the SPE Middle East Oil and Gas Show and Conference, Society of Petroleum Engineers.

Donaldson, A., and G. M. Clydesdale, 1990, Accurate reservoir evaluation quality core samples–a good starting point, *in* P. F. Worthington, ed., Advances in core evaluation: Gordon & Breach Science, 35–53.

Fink, J. K., 2015, Drilling muds, *in* J. K. Fink, ed., Petroleum engineer's guide to oil field chemicals and fluids, second ed.: Gulf Professional Publishing, 1–61.

Fullagar, P. K., D. W. Livelybrooks, P. Zhang, A. J. Calvert, and Y. Wu, 2000, Radio tomography and borehole radar delineation of the McConnell nickel sulfide deposit, Sudbury, Ontario, Canada: Geophysics, **65**, 1920–1930.

George, B. K., C. Torres-Verdin, M. Delshad, R. Sigal, F. Zouioueche, and B. Anderson, 2003, A case study integrating the physics of mud-filtrate invasion with the physics of induction logging: Assessment of in-situ hydrocarbon saturation in the presence of deep invasion and highly saline connate water: Presented at the SPWLA 44th Annual Logging Symposium, Society of Petrophysicists and Well-Log Analysts.

Giannakis, I., and A. Giannopoulos, 2014, Time-synchronized convolutional perfectly matched layer for improved absorbing performance in FDTD: IEEE Antennas and Wireless Propagation Letters, **14**, 690–693.

Giannopoulos, A., 2012, Unsplit implementation of higher order PMLs: IEEE Transactions on Antennas and Propagation, **60**, 1479–1485.

458 Glover, P., I. Zadjali, and K. Frew, 2006, Permeability prediction from MICP and NMR
459 data using an electrokinetic approach: Geophysics, **71**, no. 4, F49–F60.
460 Grude, S., J. Dvorkin, and M. Landrø, 2014, Permeability variation with porosity, pore
461 space geometry, and cement type: A case history from the Snøhvit field, the Barents Sea:
462 Geophysics, **80**, no. 1, D43–D49.
463 Gunawan, A. Y., P. Sukarno, and E. Soewono, 2011, Modeling of mud filtrate invasion and
464 damage zone formation: Journal of Petroleum Science and Engineering, **77**, 359–364.
465 Heigl, W. M., and M. Peeters, 2005, Can we obtain invasion depth with directional borehole
466 radar?: Petrophysics, **46**, 52–61.
467 Hizem, M., H. Budan, B. Deville, O. Faivre, L. Mosse, and M. Simon, 2008, Dielectric
468 dispersion: A new wireline petrophysical measurement: SPE Annual Technical
469 Conference and Exhibition, Society of Petroleum Engineers, 116130.
470 Liang, H., H. Yang, and J. Zhang, 2012, A cylindrical conformal directional monopole
471 antenna for borehole radar application: IEEE Antennas and Wireless Propagation
472 Letters, **11**, 1525–1528.
473 Liu, H., X. Huang, F. Han, J. Cui, B. F. Spencer, and X. Xie, 2019, Hybrid polarimetric
474 GPR calibration and elongated object orientation estimation: IEEE Journal of Selected
475 Topics in Applied Earth Observations and Remote Sensing.
476 Liu, S., 2014, Electromagnetic wave shielding and absorbing materials (in Chinese):
477 Chemical Industry Press.
478 Liu, S., J. Wu, H. Dong, L. Fu, and F. Wang, 2012, The experimental results and analysis
479 of a borehole radar prototype: Journal of Geophysics and Engineering, **9**, 201–209.
480 Ma, C., Q. Zhao, J. Huo, X. Chang, and L. Ran, 2016, Single borehole radar for well logging
481 in a limestone formation: Experiments and simulations: Journal of Environmental and

Engineering Geophysics, **21**, 201–213.

Miorali, M., E. Slob, and R. Arts, 2010, A feasibility study of borehole radar as a permanent downhole sensor: Geophysical Prospecting, **59**, 120–131.

Miorali, M., F. Zhou, E. Slob, and R. Arts, 2011, Coupling ground penetrating radar and fluid flow modeling for oilfield monitoring applications: Geophysics, **76**, no. 3, A21–A25.

Murphy, R., and W. Owens, 1964, Time-lapse logging, a valuable reservoir evaluation technique: Journal of Petroleum Technology, **16**, 15–19.

Navarro, D., 2007, Effects of invasion transient on resistivity time-lapsed logging: Master's thesis, University of Houston.

Nooruddin, H. A., and M. E. Hossain, 2011, Modified Kozeny–Carmen correlation for enhanced hydraulic flow unit characterization: Journal of Petroleum Science and Engineering, **80**, 107–115.

Oloumi, D., M. I. Pettersson, P. Mousavi, and K. Rambabu, 2015, Imaging of oil-well perforations using UWB synthetic aperture radar: IEEE Transactions on Geoscience and Remote Sensing, **53**, 4510–4520.

Oloumi, D., J. Ting, and K. Rambabu, 2016, Design of pulse characteristics for near-field UWB–SAR imaging: IEEE Transactions on Microwave Theory and Techniques, **64**, 2684–2693.

Salazar, J. M., and C. Torres-Verdín, 2008, Quantitative comparison of processes of oil- and water-based mud-filtrate invasion and corresponding effects on borehole resistivity measurements: Geophysics, **74**, no. 1, E57–E73.

Sato, M., and T. Miwa, 2000, Polarimetric borehole radar system for fracture measurement: Subsurface Sensing Technologies and Applications, **1**, 161–175.

Sirait, A. M. M., 2015, Permeability estimation based on cokriged porosity data: Technical

report, Indonisia.

Slob, E., M. Sato, and G. Olhoeft, 2010, Surface and borehole ground-penetrating-radar developments: Geophysics, **75**, no. 5, 75A103–75A120.

Taflove, A., and S. C. Hagness, 2005, Computational electrodynamics: The finite-difference time-domain method: Artech house.

Tang, X., and C. Cheng, 1996, Fast inversion of formation permeability from Stoneley wave logs using a simplified Biot-Rosenbaum model: Geophysics, **61**, 639–645.

Timur, A., 1968, An investigation of permeability, porosity and residual water saturation relationships for sandstone reservoirs: The Log Analyst, **9**, 8–17.

Torres-Verdín, C., F. O. Alpak, and T. M. Habashy, 2006, Petrophysical inversion of borehole array-induction logs: Part II–Field data examples: Geophysics, **71**, no. 5, G261–G268.

Tronicke, J., K. Holliger, W. Barrash, and M. D. Knoll, 2004, Multivariate analysis of cross-hole georadar velocity and attenuation tomograms for aquifer zonation: Water Resources Research, **40**, W01519.

Van Lookeren, J., 1965, Oil production from reservoirs with an oil layer between gas and bottom water in the same sand: Journal of Petroleum Technology, **17**, 354–357.

Warren, C., A. Giannopoulos, and I. Giannakis, 2016, gprmax: Open source software to simulate electromagnetic wave propagation for ground penetrating radar: Computer Physics Communications, **209**, 163–170.

Weller, A., S. Nordsiek, and W. Debschütz, 2010, Estimating permeability of sandstone samples by nuclear magnetic resonance and spectral-induced polarization: Geophysics, **75**, no. 6, E215–E226.

Wu, J., Torres-Verdin, K. Sepehrnoori, and M. A. Proett, 2005, The influence of water-base

mud properties and petrophysical parameters on mudcake growth, filtrate invasion, and formation pressure: Petrophysics, **46**, 14–32.

Yao, C., and S. Holditch, 1993, Estimating permeability profiles using core and log data: Presented at the SPE Eastern Regional Meeting, Society of Petroleum Engineers.

Zhao, J., and M. Sato, 2006, Radar polarimetry analysis applied to single-hole fully polarimetric borehole radar: IEEE Transactions on Geoscience and Remote Sensing, **44**, 3547–3554.

Zhou, F., 2011, Reservoir dynamic monitoring using borehole radar and its application in smart well production: PhD thesis, China University of Geosciences (Wuhan).

Zhou, F., X. Hu, Q. Meng, X. Hu, and Z. Liu, 2015, Model and method of permeability evaluation based on mud invasion effects: Applied Geophysics, **12**, 482–492.

Zhou, F., Q. Meng, X. Hu, E. Slob, H. Pan, and H. Ma, 2016, Evaluation of reservoir permeability using array induction logging: Chinese Journal of Geophysics, **59**, 703–716.

Zhou, F., M. Miorali, E. Slob, and X. Hu, 2018, Reservoir monitoring using borehole radars to improve oil recovery: Suggestions from 3D electromagnetic and fluid modeling: Geophysics, **83**, no. 2, WB19–WB32.

Zhou, H., and M. Sato, 2004, Subsurface cavity imaging by crosshole borehole radar measurements: IEEE Transactions on Geoscience and Remote Sensing, **42**, 335–341.

Zunker, F., 1930, Das verhalten des bodens zum wasser, *in* A. Densch, F. Giesecke, M. Helbig, V. F. Hess, J. Schubert, F. Zunker ed., Die Physikalische Beschaffenheit des Bodens: Springer, 66–220.

LIST OF FIGURES

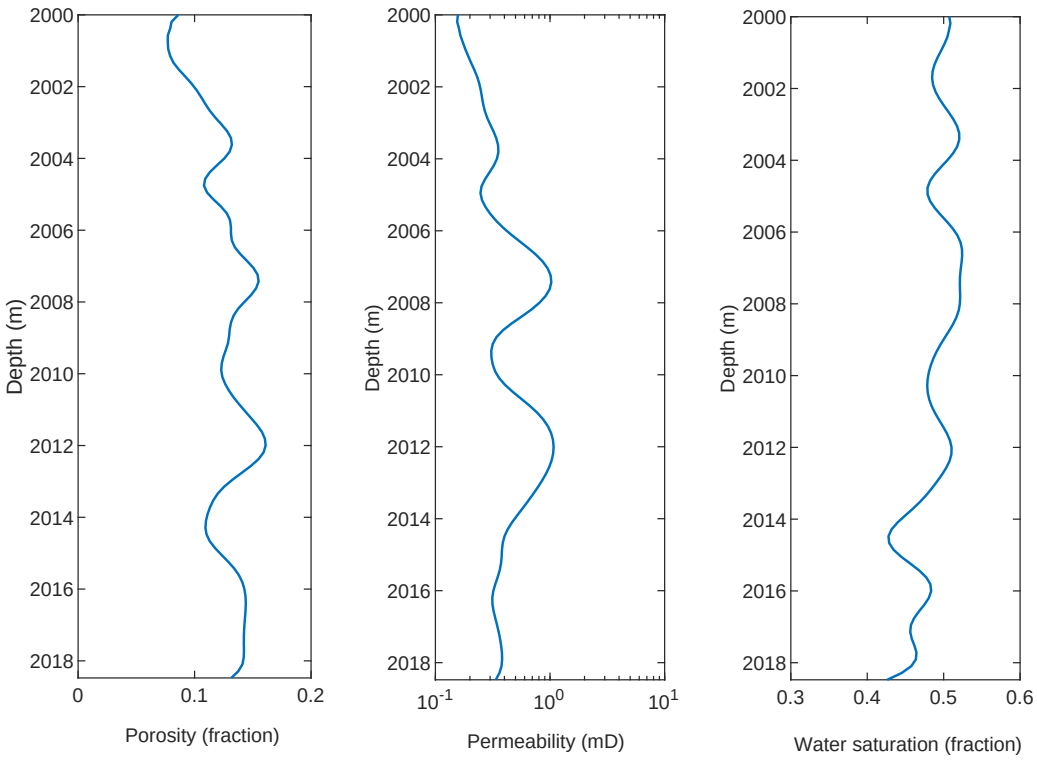

(a) (b) (c)

Figure 1: Porosity, permeability, and water saturation curves based on the coring data from a well in the Honghe Oilfield, Ordos, China. The data have been smoothed using a 5-point moving average filter.

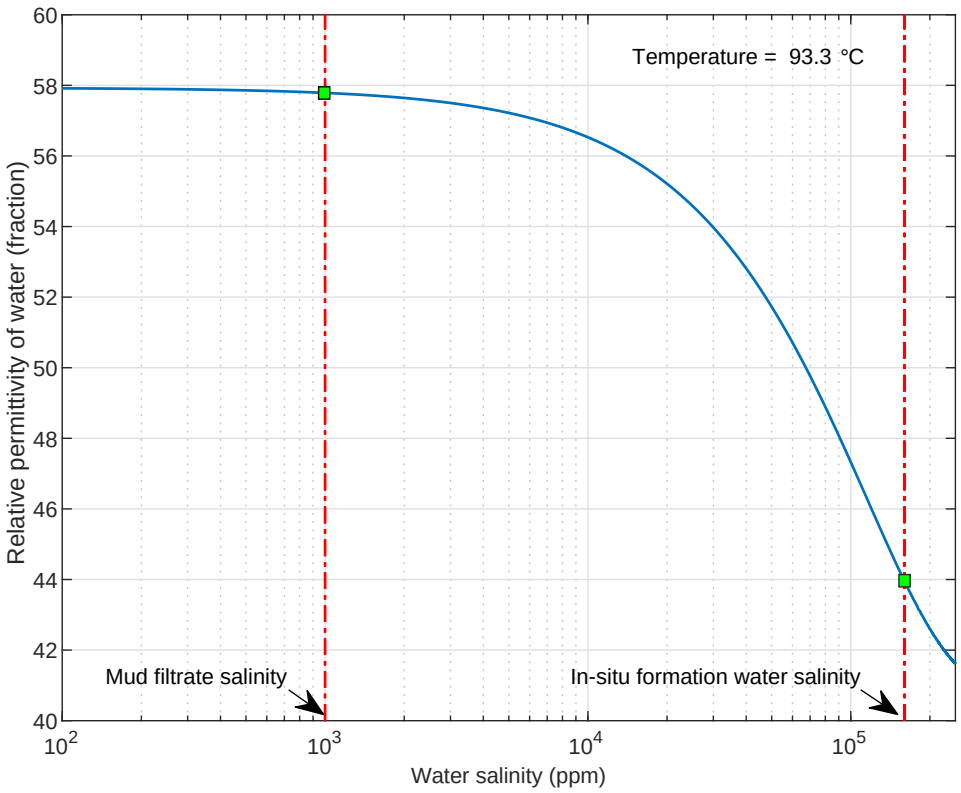

Figure 2: Relative permittivity of water as a function of salinity at the temperature of the simulated reservoir for the frequency of 1 GHz.

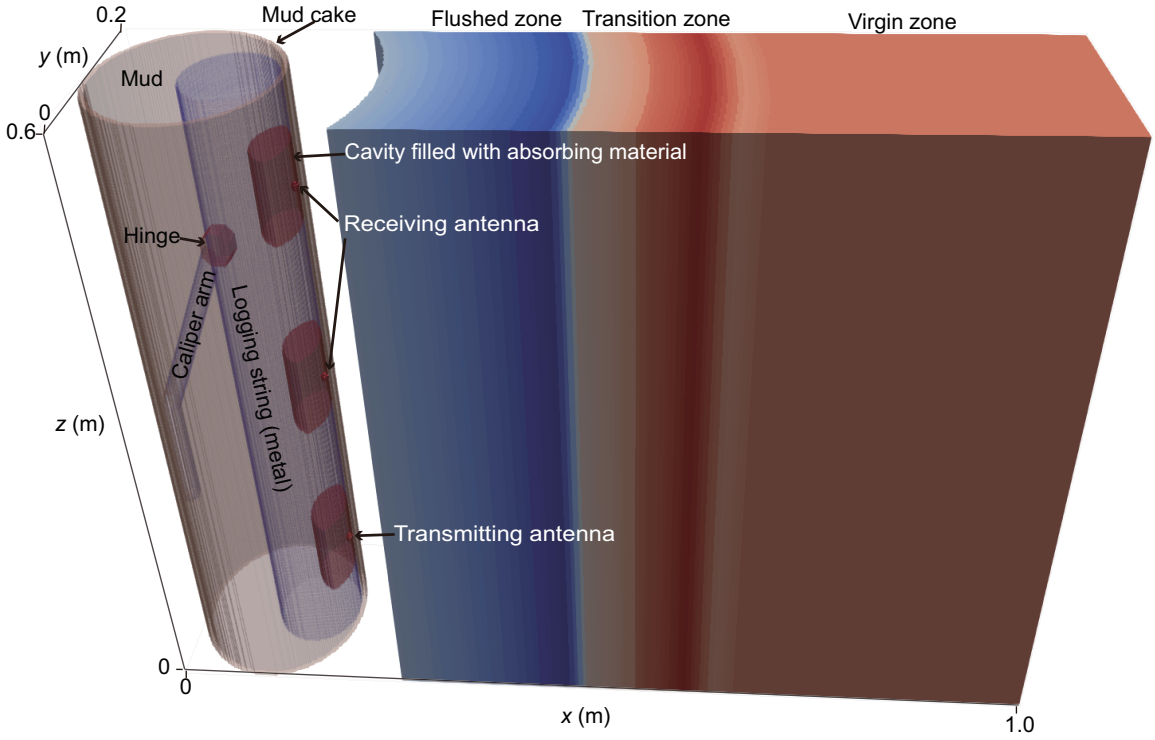

Figure 3: Schematic presentation of borehole radar model configuration and fluid distribution. Colors denote the materials with different electrical properties.

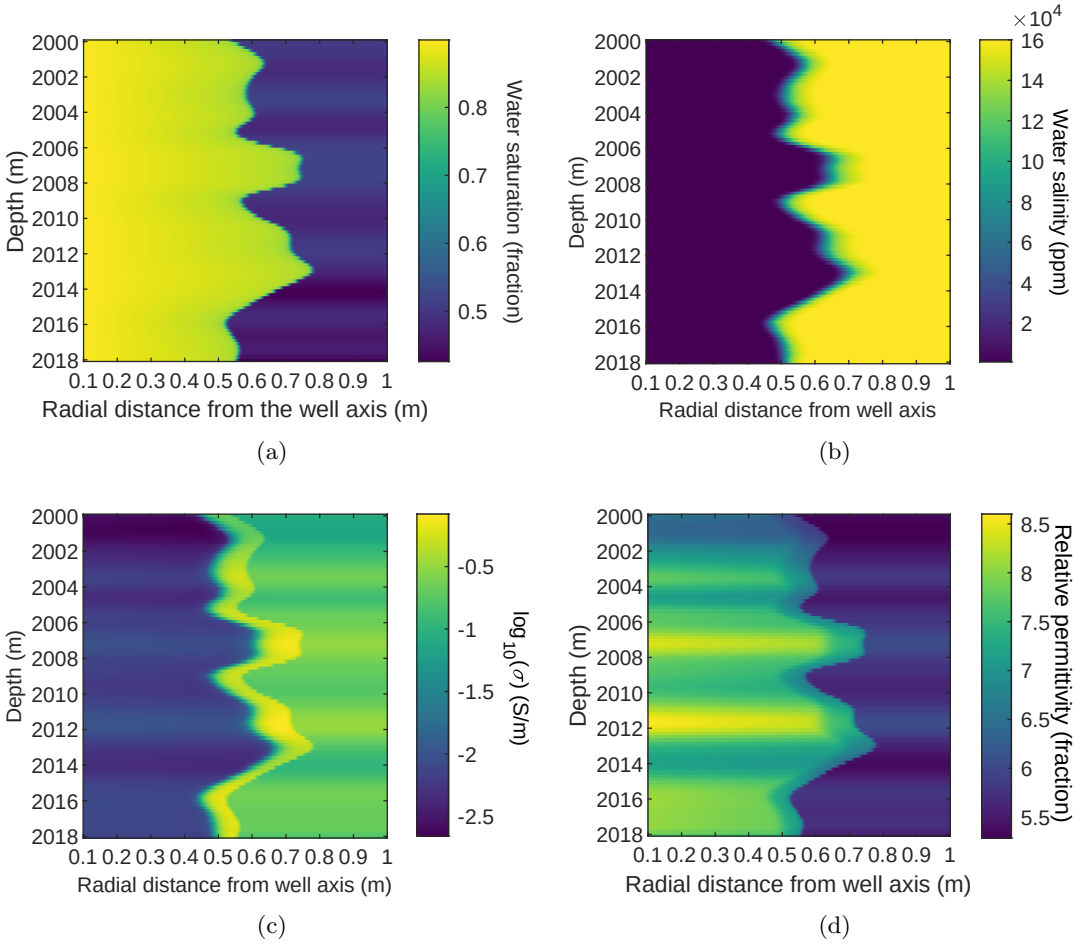

Figure 4: 2D distributions of water saturation (a), water salinity (b), bulk conductivity (c), and bulk relative permittivity (d) after 36 hours of invasion. Note that the x-axis starts from the borehole wall.

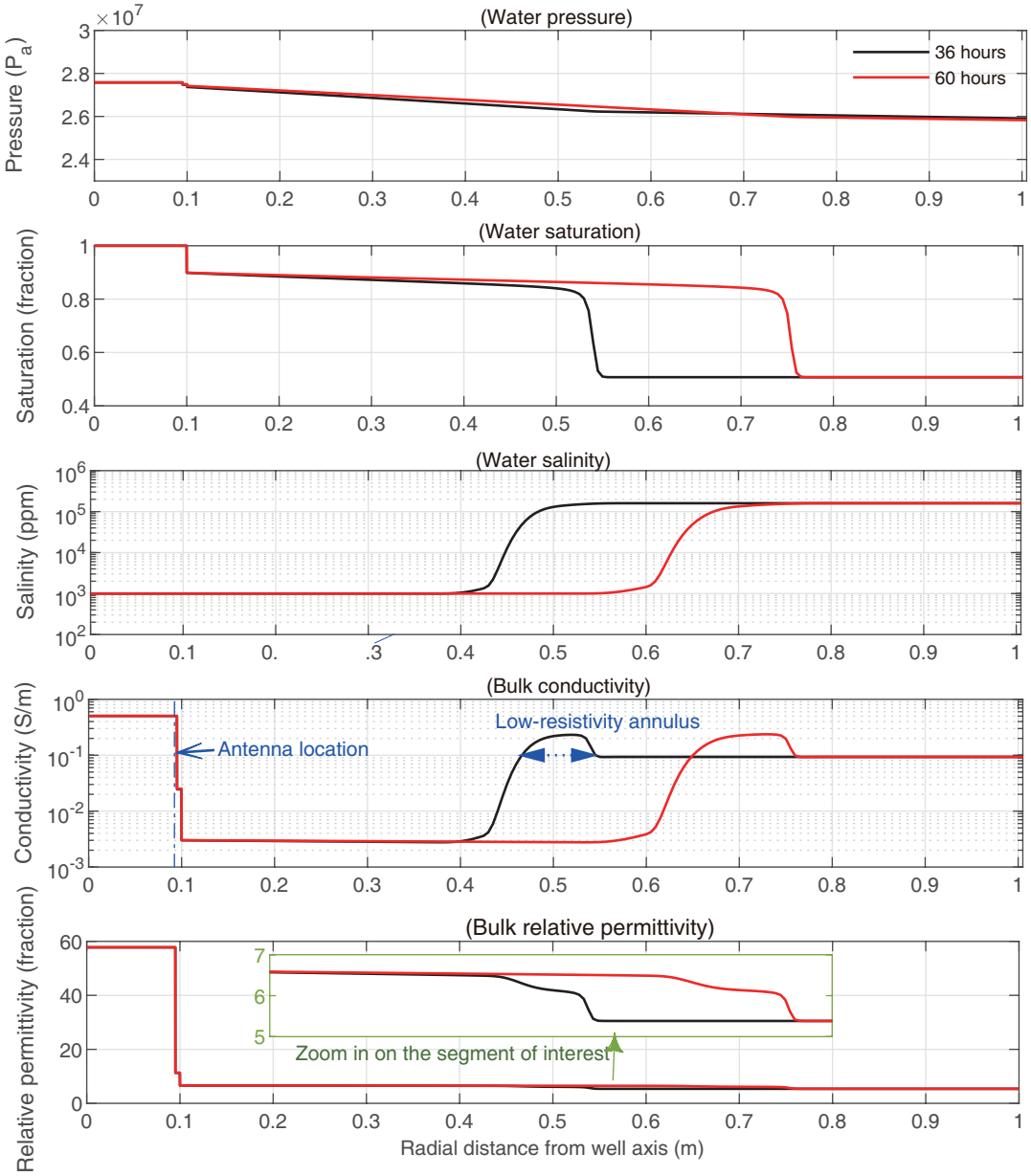

Figure 5: Radial distributions of water pressure, water saturation, water salinity, bulk conductivity, and bulk relative permittivity after 36 (black curves) and 60 hours (red curves) of invasion, respectively. The 1D curves are extracted from the simulated data at a depth of 2000 m. The radial ranges of 0–0.95 m and 0.95–1 m denote the borehole and mud cake parts, respectively.

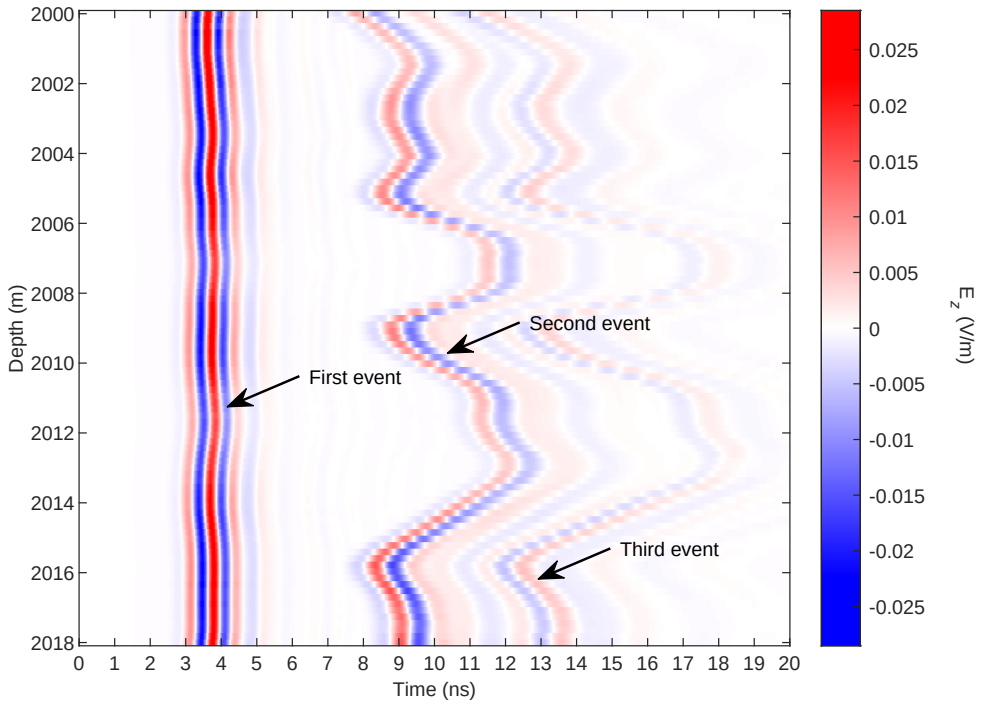

(a)

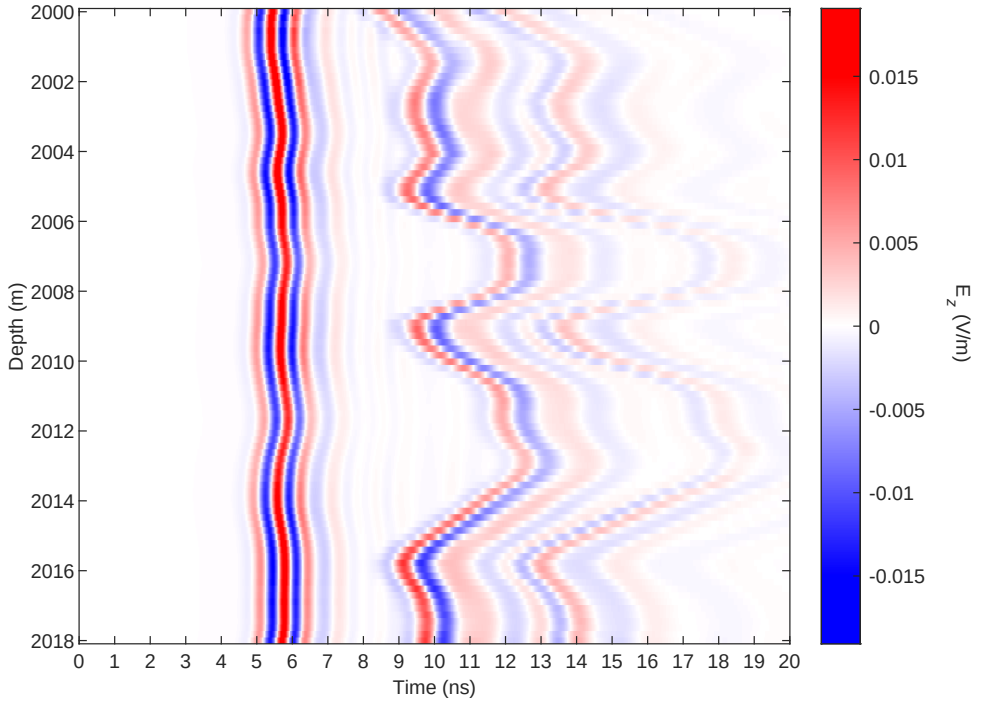

(b)

Figure 6: Time-lapse radar profile acquired by the first (a) and second (b) receiving antennas with the measurements after 36 and 60 hours of invasion, respectively.

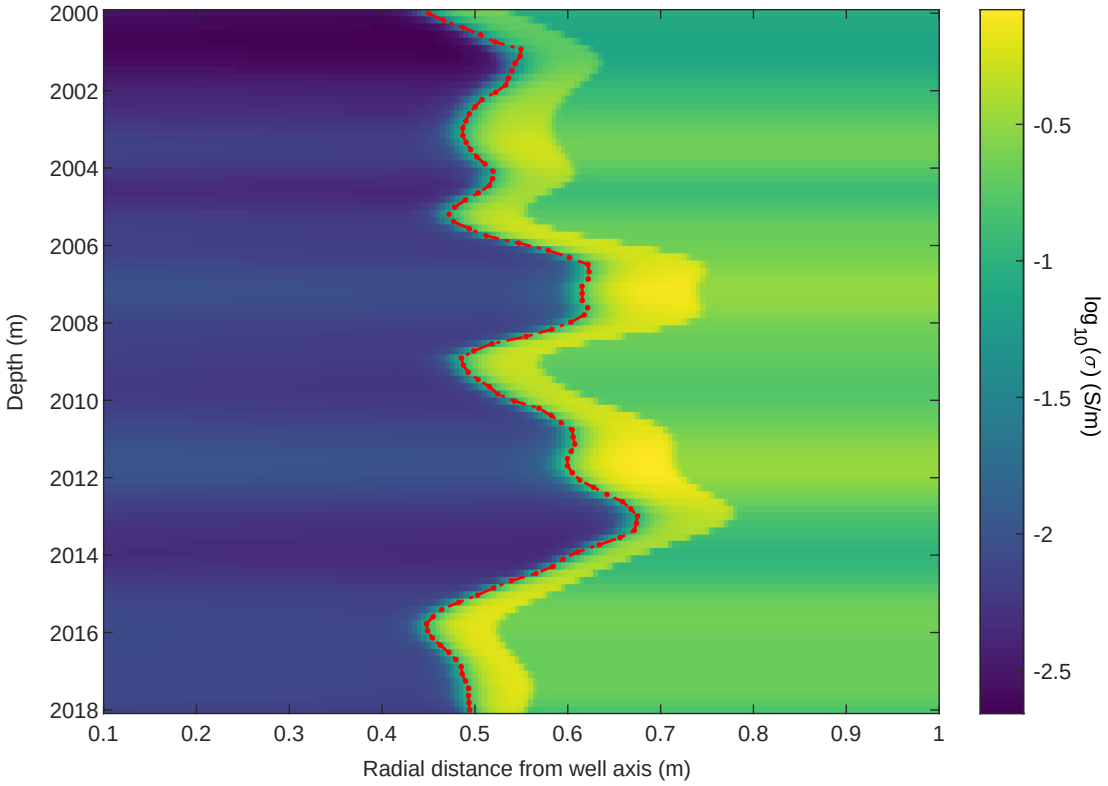

Figure 7: Radar-estimated invasion depth versus the simulated conductivity distribution after 36 hours of invasion. The red dotted line presents the invasion depth estimated by borehole radar data, and the varying colors denote the electrical conductivity on a logarithmic scale.

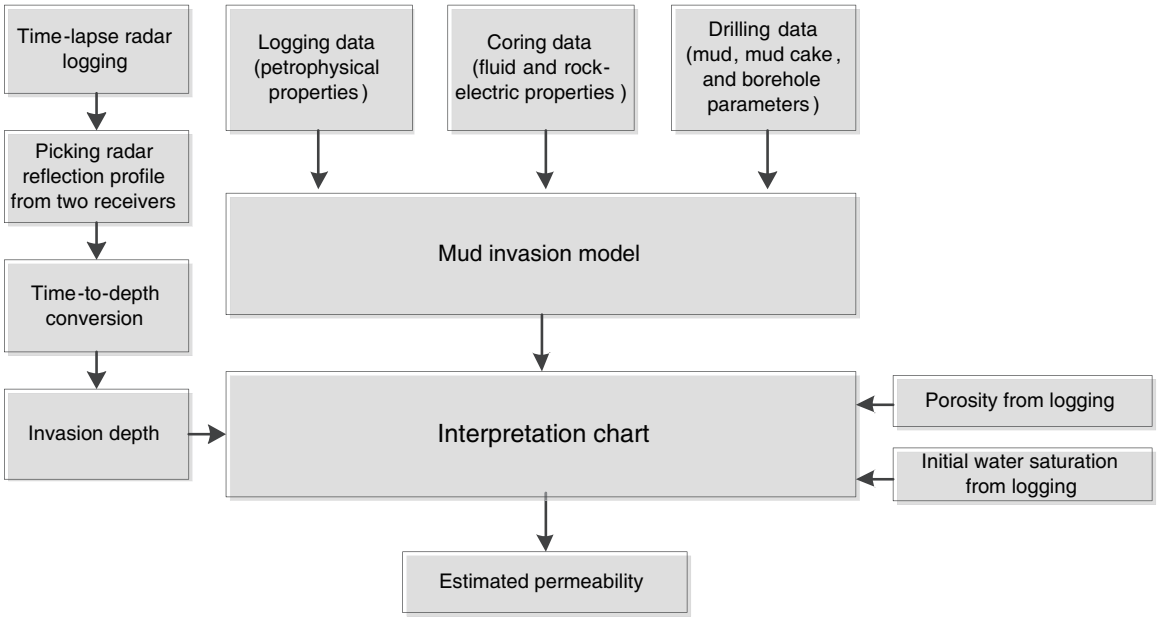

Figure 8: Flow chart illustrating the estimation of permeability based on borehole radar measurements.

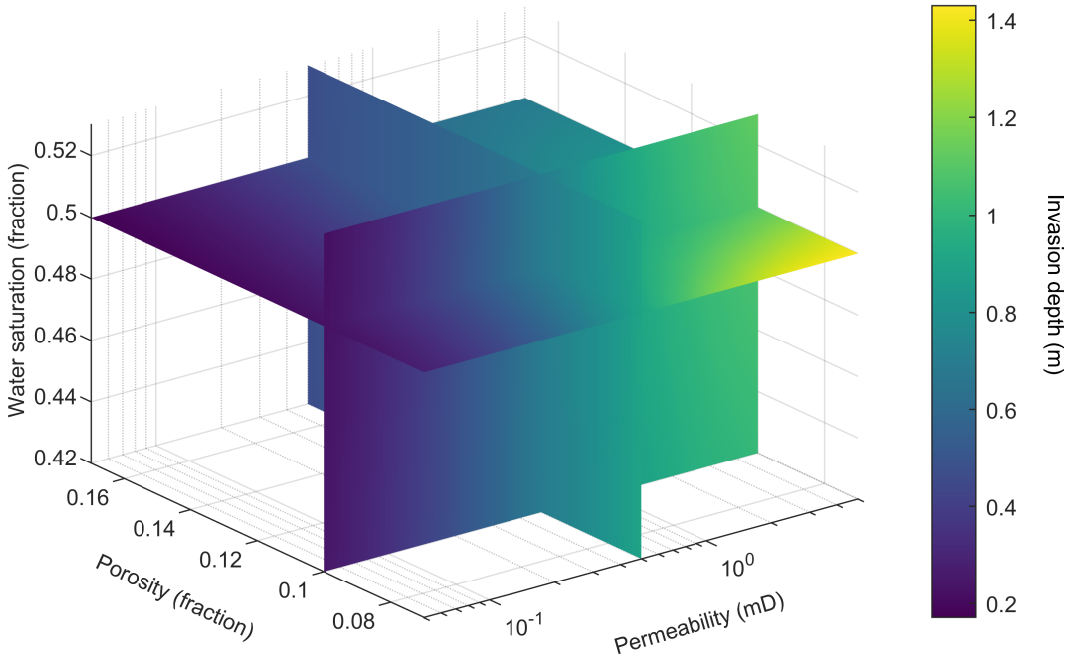

Figure 9: 4D interpretation chart presented by slices associating invasion depth with porosity, permeability, and initial water saturation after 36 hours of invasion for the reservoir scenario defined in Table 1.

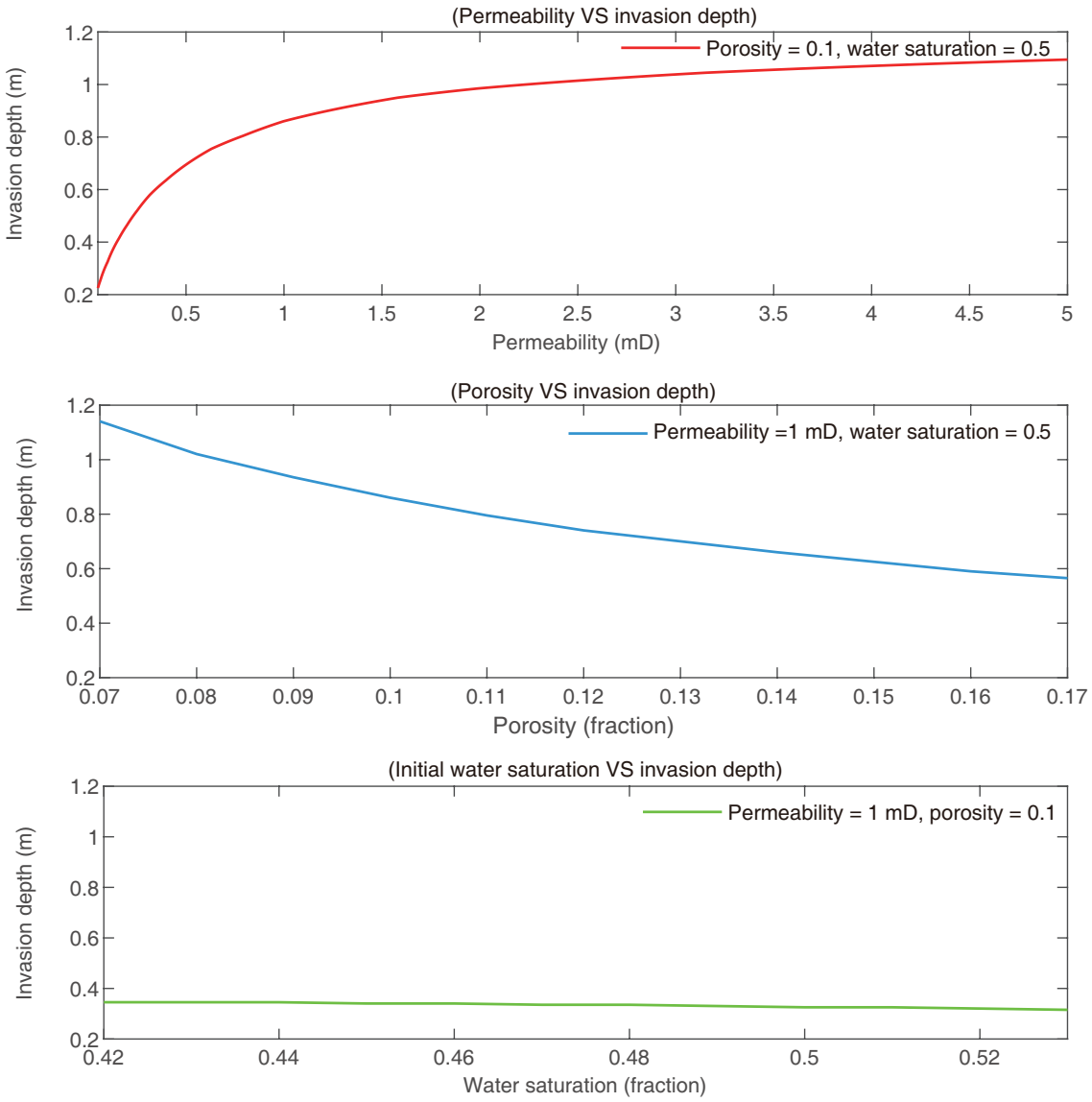

Figure 10: 1D curves extracted from Figure 9 associating invasion depth with permeability, porosity, and initial water saturation.

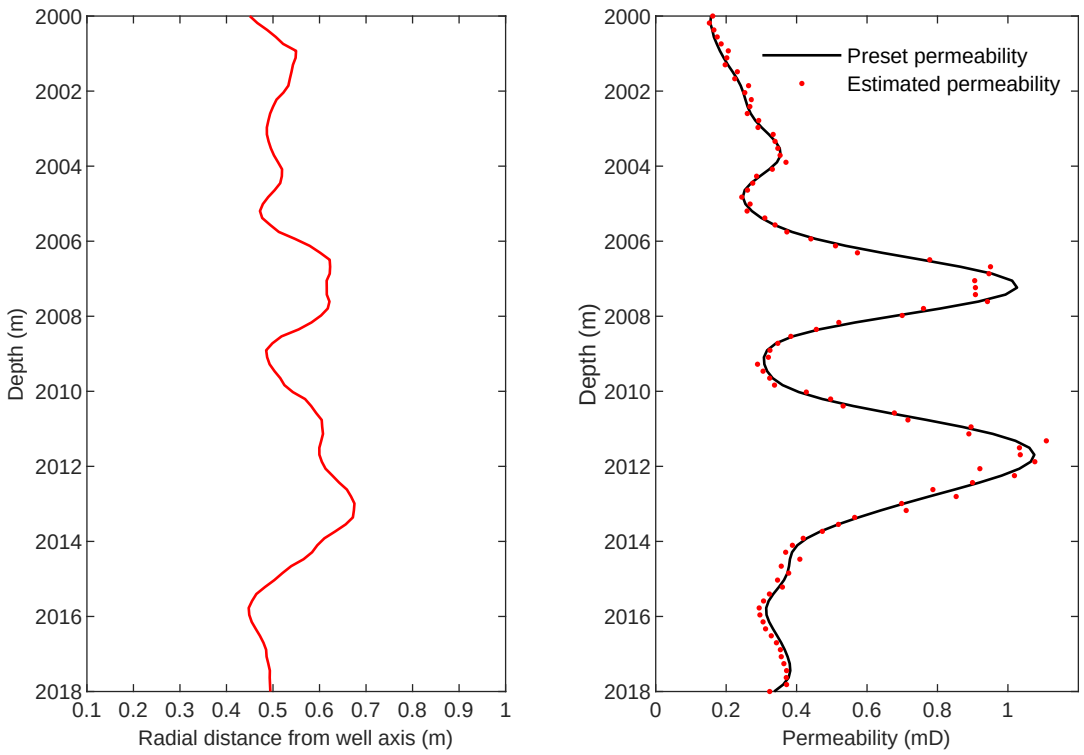

(a) (b)

Figure 11: Invasion depth acquired through borehole radar (a) and the comparison between the estimated and preset permeability curves (b).

LIST OF TABLES

Table 1: Drilling, fluid, and reservoir properties (Alpak et al., 2006; Navarro, 2007; Salazar and Torres-Verdín, 2008).

Variables	*Values*	*Units*
Wellbore radius	0.10	m
Mud hydrostatic pressure	27580	kPa
Mud cake maximum thickness	0.005	m
Mud filtrate salinity	1×10^3	ppm
Mud density	1130	kg/m^3
Mud cake reference permeability	0.05	md
Mud cake reference porosity	0.25	fraction
Mud solid fraction	0.06	fraction
Mud cake compressibility exponent	0.4	fraction
Mud cake exponent multiplier	0.1	fraction
Formation pressure	25166	kPa
Formation water salinity	160×10^3	ppm
Formation temperature	93.3	°C
Water density	1001	kg/m^3
Oil density	816	kg/m^3
Water viscosity	1.274×10^{-3}	Pa·s
Oil viscosity	0.355×10^{-3}	Pa·s
Rock compressibility	7.252×10^{-10}	1/kPa
Water compressibility	3.698×10^{-7}	1/kPa
Oil compressibility	2.762×10^{-6}	1/kPa
Connate water saturation	0.15	fraction
Residual oil saturation	0.10	fraction
Endpoint relative permeability of water	0.3	fraction
Endpoint relative permeability of oil	1	fraction
Empirical exponent of water relative permeability	2	fraction
Empirical exponent for oil relative permeability	2	fraction
Capillary pressure coefficient	1.87	Pa·cm
Empirical exponent for pore-size distribution	20	fraction
Diffusion coefficient of salt	6.45×10^{-9}	m^2/s
Dispersion coefficient of salt	1.3×10^{-3}	m
Horizontal and vertical ratio of formation permeability	10	fraction

Table 2: Geometric parameters and electrical properties for borehole radar and reservoir models.

Variables	*Values*	*Units*
Logging string radius	0.05	m
First transmitter−receiver spacing	0.20	m
Second transmitter−receiver spacing	0.40	m
Radial depth of cavity	0.04	m
Longitudinal length of cavity	0.08	m
Real part of relative permittivity of absorbing material	20	fraction
Imaginary part of relative permittivity of absorbing material	9	fraction
Real part of magnetic permeability of absorbing material	1.2	fraction
Imaginary part of magnetic permeability of absorbing material	12	fraction
Tortuosity factor	1	fraction
Cementation exponent	2	fraction
Saturation exponent	2	fraction
Relative permittivity of oil	2	fraction
Relative permittivity of dry sandstone	4.65	fraction
Relative permittivity of water at 93.3 °C	57.93	fraction